Characterizing variability and vertical structure of water vapor in the extratropical lower stratosphere

Emily N. Tinney and William J. Randel

National Center for Atmospheric Research, Boulder, CO, USA

Correspondence: Emily N. Tinney (etinney24@ucar.edu)

Abstract. Stratospheric water vapor strongly affects Earth's radiative balance, especially in the extratropical lower stratosphere, yet large uncertainties remain regarding its variability, long-term trends and relationships to tropopause behavior. Here we characterize the seasonality, vertical structure, and variability of water vapor near the extratropical tropopause and the extratropical transition layer (ExTL). We analyze 17 years (2005–2021) of satellite observations from the Aura Microwave Limb Sounder (MLS) and the Atmospheric Chemistry Experiment Fourier transform spectrometer (ACE-FTS), with simulations from the Whole Atmosphere Community Climate Model (WACCM) using specified dynamics calculations. Analyses are performed in geometric and tropopause-relative vertical coordinates to assess the influence of coordinate on variability. Tropopause-relative coordinates substantially reduce variance in ExTL water vapor, but artificially enhance variability in the tropical upper troposphere. Tropopause-relative coordinates reveal a clear distinction between variability in the ExTL and the stratospheric overworld approximately 2.5 km above the tropopause. Above this level, there are hemispherically coherent anomalies linked to transport of air originating in the tropics. In contrast, ExTL variability lacks hemispheric coherence and likely reflects smaller-scale stratosphere-troposphere exchange. Interannual changes in ExTL water vapor show a statistically significant negative trend in both hemispheres in MLS data, but that behavior is not reproduced in ACE-FTS measurements or WACCM simulation. Despite this, the datasets agree well on overworld variability and regression responses to climate oscillations. The uncertainty in ExTL trends highlights the need for continued evaluation of long-term satellite records and improved model representation in this climatically sensitive layer.

1 Introduction

Stratospheric water vapor (H_2O) is a critical component of Earth's radiative budget, and despite extremely low values relative to the troposphere even small changes in its concentration can have outsized impacts on surface temperatures and stratospheric circulation (Charlesworth et al., 2023; Solomon et al., 2010; Forster and Shine, 2002). H_2O in the extratropical lower stratosphere is especially important for radiative feedbacks (Charlesworth et al., 2023; Li and Newman, 2020; Banerjee et al., 2019; Dessler et al., 2013), although the magnitude of such a feedback is still debated and results can depend on the models and method used in the calculation (He and Huang, 2025). The tropopause in the extratropics is a complex transition region between the troposphere and stratosphere, with strong gradients in H_2O, ozone, and other constituents and an interplay of large-

25 and small-scale circulations and radiative processes; this transition region is often referred to as the Extratropical Transition
Layer (ExTL; e.g., Gettelman et al., 2011).

When studying stratospheric H_2O it can be useful to separate the stratosphere into different regions due to the underlying
controlling processes and modes of transport. Specifically, the stratosphere is frequently divided into the stratospheric over-
world and the (extratropical) lowermost stratosphere. The stratospheric overworld is conventionally defined as the region of
30 the stratosphere above the 380 K isosurface of potential temperature, where composition is controlled by a source region near
the tropical tropopause and the stratospheric transport circulation (Stohl et al., 2003; Holton et al., 1995; Hoskins, 1991). The
lowermost stratosphere (LMS; also called the 'middleworld') is the region in extratropics that exists below the 380 K isentrope
but above the extratropical tropopause. Isentropes in the extratropical LMS cross into the tropical upper troposphere, but the
subtropical jet acts as an effective transport barrier between these regions (Haynes et al., 2001). Overworld H_2O is controlled by
35 two main processes: upward transport through the tropical tropopause via the Brewer-Dobson Circulation (BDC; e.g., Butchart,
2014) and methane oxidation in the upper stratosphere (Tao et al., 2023; Yu et al., 2022). Air is freeze dried as it ascends into
the stratosphere and the temperature of the tropical tropopause controls H_2O concentrations. Randel and Park (2019) demon-
strated that tropical cold point temperatures (CPT) explain more than $\sim$80% of the variability in global stratospheric overworld
H_2O concentrations. Variations in CPT then leave a vertically and horizontally propagating imprint on overworld stratospheric
40 H_2O, commonly referred to as the 'atmospheric tape recorder' (Mote et al., 1996). Alternatively, transport in the LMS is more
complex, where stratosphere-troposphere exchange can be facilitated by Rossby wave breaking events, tropospheric intrusions,
midlatitude cyclones, and tropopause-overshooting convection (e.g., Chang et al., 2023; Tinney and Homeyer, 2021; Homeyer
and Bowman, 2013; Homeyer et al., 2011; Pan et al., 2009; Olsen et al., 2008). These processes complicate H_2O variability
in the LMS, and their relative contributions are not well understood. A further complicating factor is the large variation in the
45 tropopause structure itself on timescales of days to decades, including a large seasonal cycle in midlatitudes. Global observa-
tions of stratospheric water vapor are primarily collected by satellites with relatively low horizontal and vertical resolution,
further limiting study of this region. Another complication is that global circulation models routinely overestimate the amount
of LMS H_2O in historical and present climates (Charlesworth et al., 2023), contributing to poor understanding of this region.

The objective of this work is to analyze the seasonal and interannual variability and vertical structure of stratospheric H_2O in
50 the LMS and across the ExTL using satellite observations and a global chemistry-climate model. Specifically, we use a 17-year
period of observations from the Aura Microwave Limb Sounder (MLS) and SCISAT-1's Atmospheric Chemistry Experiment
Fourier transform spectrometer (ACE-FTS) in conjunction with simulations using the Whole Atmosphere Community Climate
Model (WACCM) run in specified dynamics mode with observed meteorological fields. We aim to quantify variability and
highlight the role of different sources in shaping the distribution of H_2O throughout the LMS. A key aspect of this work
55 includes analysis in tropopause-following coordinates, in addition to standard geometric coordinates.

2 Data and Methods

2.1 MLS

Measurements of water vapor, ozone, and temperature from 2005 – 2021 are sourced from the Earth Observing System (EOS) MLS aboard the Aura satellite, version 5.0x. Aura was launched in 2004 into a sun-synchronous satellite orbit with Equator crossing times of 1:30 and 13:30 local time as part of the NASA A-Train satellite constellation. MLS measures ∼3600 profiles per day with a 1.5° along-track separation between measurements (Livesey et al., 2022). The retrieval range of MLS measurements vary by species; water vapor is observed from 316 – 0.001 hPa, ozone from 261 – 0.001 hPa and temperature from 261 – 0.00046 hPa. Retrievals are provided on a regular pressure grid, with data at 12 levels per decade of pressure (∼1.25 km vertical sampling) for pressures greater than 1 hPa. The precision, accuracy, horizontal resolution, and vertical resolution of each species vary by altitude and are described in detail in Livesey et al. (2022). In our region of focus in the UTLS, the effective vertical resolution is ∼3 km for water vapor and ozone. The data analyzed here are monthly, zonal averages binned in 2-degree latitude bins, which contain on the order of 1000 measurements per month over midlatitudes.

2.2 ACE-FTS

We also analyze satellite water vapor observations from the ACE-FTS (hereafter ACE) instrument from 2005 – 2021, using the version 5.2 retrieval (Bernath et al., 2005). ACE measures solar occultation spectra between 750 and 4400 cm^{-1} at a spectral resolution of 0.02 cm^{-1} to retrieve vertical profiles of temperature, pressure, and trace gas volume mixing ratios from the cloud tops to approximately 150 km. Altitude is the native vertical coordinate for these retrievals and the effective vertical resolution in the UTLS is about 3 km, oversampled at 1 km spacing. The instrument typically measures 30 profiles per day, requiring a three-month period to achieve near-global coverage (85°N – 85°S). The recommended ACE v5.2 quality-control flags described in Sheese et al. (2015) are applied to remove scientifically unsuitable profiles prior to analysis. We perform an additional simple quality control measure to eliminate extreme and non-physical measurements (particularly near and below the tropopause) from the dataset by removing data points that fall outside of the 2nd and 98th percentile values for their specific height and latitudinal region. Because of the much sparser sampling of ACE compared to MLS, we use 3-month (DJF, MAM, etc.) averages in 10-degree latitude bins, which typically contain ∼20 – 100 measurements over midlatitudes. We require a minimum of 10 data points per 3-month 10-degree latitude bin for a valid data sample. Because of frequent loss of ACE-FTS retrievals below the tropopause (due to clouds or other problems) there are often missing data, and these regions are indicated as data voids in the figures below.

2.3 WACCM

Numerical experiments were conducted using the Community Earth System Model version 2 with the Whole Atmosphere Community Climate Model version 6 as its atmospheric component (CESM2/WACCM6; Danabasoglu et al., 2020; Gettelman et al., 2019). WACCM6 is a state-of-the-art chemistry–climate model that extends from the Earth's surface to approximately
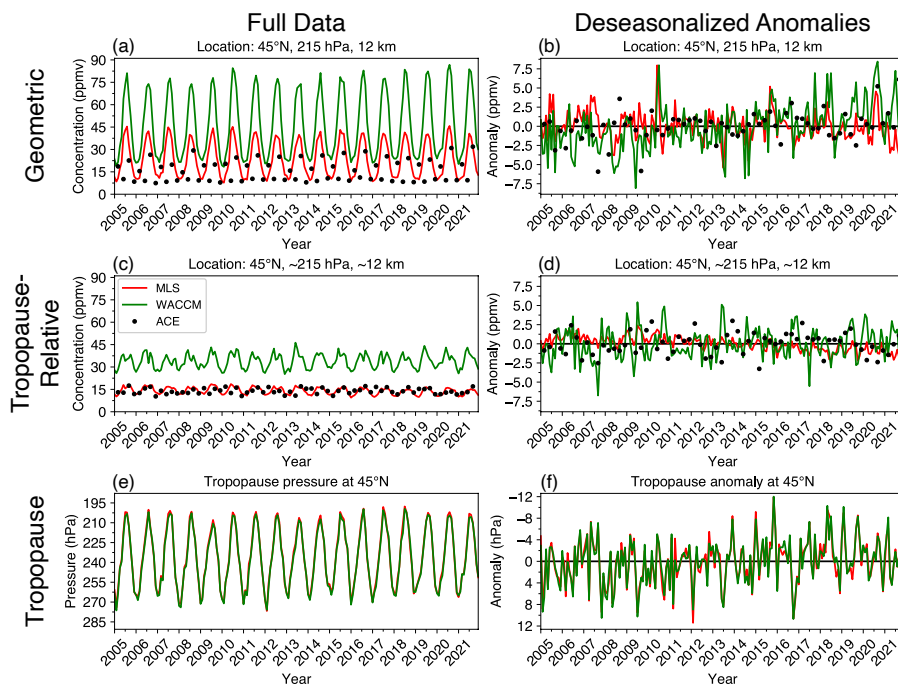
Figure 1. Upper and middle panels show time series of zonal mean H_2O at 45 N, 215 hPa (12 km), close to the midlatitude tropopause, from MLS data (red), ACE data (black dots), and WACCM simulation (green). (a) time series in geometric coordinates, (b) time series in tropopause-relative coordinates. Variations in tropopause pressure are shown in (c). Panels (d-f) show the corresponding deseasonalized anomalies.

140 km and includes comprehensive troposphere–stratosphere–mesosphere–lower thermosphere (TSMLT) chemistry. In this study, WACCM6 is run in a specified-dynamics configuration (WACCM6-SD), with prescribed sea surface temperatures and sea ice. The simulations provide daily data covering the period 1980 – 2022 and use a horizontal resolution of 0.9° latitude x

90   1.25° longitude with the finite-volume dynamical core (Lin and Rood, 1996). The model includes 70 vertical levels from the surface to ∼140 km, with a vertical resolution of approximately 500 m in the upper troposphere and lower stratosphere (UTLS). In the specified-dynamics configuration, temperature and winds (U, V) are nudged toward the Modern-Era Retrospective Analysis for Research and Applications Version 2 (MERRA-2) reanalysis (Gelaro et al., 2017) using a 12-hour relaxation timescale. This configuration has been shown to realistically reproduce key modes of stratosphere–troposphere coupling, including the

95   quasi-biennial oscillation and stratospheric sudden warmings. It also provides a realistic representation of large-scale transport in the UTLS region and has been widely used in troposphere–stratosphere transport studies (e.g., Zhang et al., 2025; Pan et al., 2022; von Hobe et al., 2021). For a direct comparison with MLS, we restrict the analysis to 2005 – 2021, interpolate to the MLS vertical grid, and compute monthly, zonal averages in 2° latitude bins.

2.4 Tropopause-relative coordinates

100 Studies of UTLS composition can benefit from analyses using alternative coordinate systems, both vertically and horizontally (Millán et al., 2024). Various vertical coordinate systems can be used to reduce the composition variability associated with changes in tropopause height to isolate other sources of variability, such as from stratosphere-troposphere exchange. For analysis of H_2O in the lowermost stratosphere, tropopause-relative altitude is a common vertical coordinate and has been frequently used in previous studies (e.g., Tinney and Homeyer, 2021; Bland et al., 2021; Schwartz et al., 2015; Gettelman et al., 2011; 105 Tilmes et al., 2010; Pan et al., 2004).

In this study we conduct analyses in both geometric (e.g. pressure, altitude) and tropopause-relative coordinates. Tropopause-relative calculations are computed for daily observations before aggregating the results into monthly (MLS, WACCM) or 3-monthly (ACE) means. For ACE and MLS, a reference tropopause is computed from three-hourly MERRA-2 reanalysis data and interpolated in space and time to each profile location (Gelaro et al., 2017). The tropopause is also calculated daily in 110 WACCM6 as the reference for the model profiles. Since the model is nudged to MERRA-2, these two tropopause datasets are nearly identical. The results shown here use the potential temperature gradient tropopause (PTGT; Tinney et al., 2022) as the reference tropopause definition. We also tested tropopause-relative calculations using the World Meteorological Organization (WMO; World Meteorological Organization, 1957) lapse-rate tropopause definition, finding consistent results with the PTGT (not shown). For MLS and WACCM, data is placed into tropopause-relative logarithmic pressure bins with a resolution 115 corresponding to 12 levels per decade of pressure ($\Delta z \sim 1.25$ km), while ACE observations are placed into to 1-km tropopause-relative altitude bins. Monthly zonal means are then computed for MLS and WACCM data and three-monthly seasonal means are computed for ACE. The tropopause-relative vertical coordinates are transformed back into an estimated geometric coordinate using the climatological mean tropopause pressure, with the logarithmic pressure bins becoming a 'pseudo-pressure' coordinate. Some of our results include (area-weighted) extratropical tropopause averages, including monthly/seasonal data 120 points poleward of 20°N/S where the local tropopause pressure exceeds 150 hPa, indicative of the lower-tropopause (extratropical) environments poleward of the tropopause break (Boothe and Homeyer, 2017; Homeyer and Bowman, 2013; Randel et al., 2007). This requirement constrains the analysis to at least partially exclude summer monsoon anticyclones, which frequently exhibit tropopause pressures of < 150 hPa (Liu et al., 2014).

An example of the H_2O variability compared in geometric vs. tropopause-relative coordinates is illustrated in Figs. 1a-125 b, showing time series of MLS, ACE, and WACCM data at one location near the midlatitude tropopause (45° N, 215 hPa, 12 km). In geometric coordinates (Fig. 1a) there is a large annual cycle of H_2O with maxima during boreal summer, which closely follows the well-known annual cycle in midlatitude tropopause pressure (Fig. 1c). Time series in tropopause-relative coordinates (Fig. 1b) show a much smaller annual cycle, with smaller maxima during boreal summer. The comparisons in Figs. 1a-b show larger H_2O values near the extratropical tropopause for WACCM compared to MLS and ACE, and this is a general 130 behavior as shown and discussed further below.

Time series of the respective deseasonalized anomalies are shown in Figs. 1d-f. Tropopause-relative calculations (Fig. 1e) show a reduction in H_2O variance compared to geometric coordinates (Fig. 1d), due to removal of variability tied to the
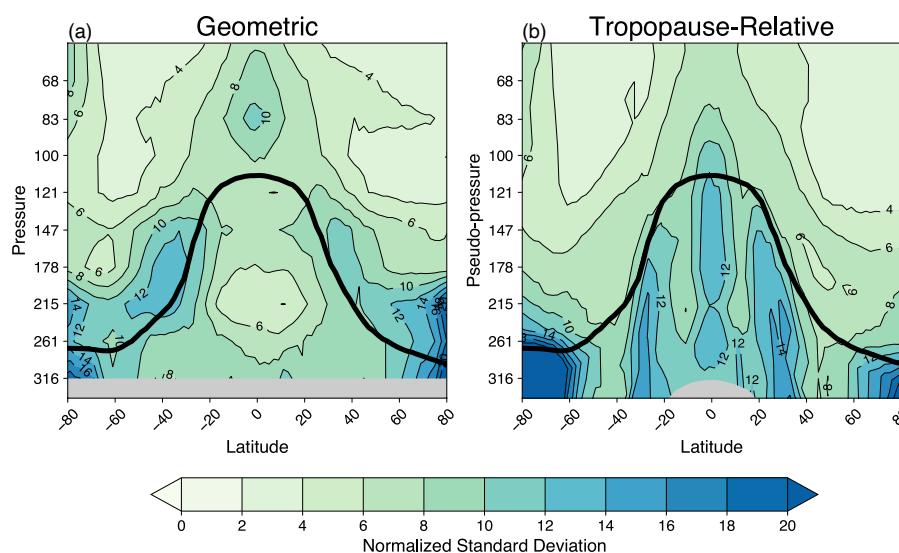
Figure 2. The normalized standard deviation for deseasonalized MLS H_2O anomalies in (a) geometric and (b) tropopause-relative coordinates. Values are in % compared to the time average background H_2O. The average height of the PTGT is shown as the solid black line.

dynamic tropopause. Figure 2 shows global comparisons of deseasonalized H_2O variance in the two coordinate systems. In geometric coordinates (Fig. 2a) there are maxima concentrated around the ExTL region of both hemispheres concentrated
135   in the ExTL region, primarily linked with variations in the tropopause itself. Calculations in tropopause-relative coordinates (Fig. 2b) substantially reduce the ExTL variability, as the variance associated with changes in the height of the tropopause is removed.

In contrast to the reduction of variance near the ExTL, the use of tropopause-relative coordinates substantially increases H_2O variability throughout the tropical upper troposphere (Fig. 2b - note maxima near 30o N and S and near the equator). This is
140   an artifact of the tropopause-relative coordinate calculations. The tropical upper troposphere is characterized by strong vertical gradients in water vapor concentration, and small variations in tropopause altitude can lead to large changes in tropopause-relative water vapor. We find that much of the enhanced H_2O variance in this region is due to low frequency changes in tropopause height tied to ENSO and QBO variations (Randel et al., 2000). As a result, using tropopause-relative coordinates introduces artificial H_2O variability in the tropical upper troposphere, and is a poor coordinate choice for this region. However,
145   this has minimal impact on our results focused on the extratropics.
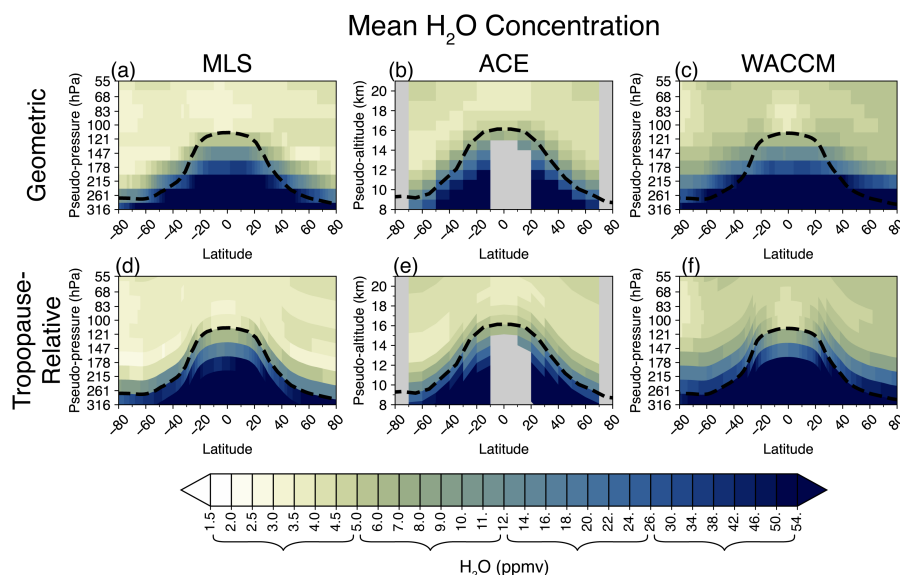
Figure 3. Time average H_2O from MLS, ACE and WACCM (left to right), analyzed in geometric (top row) and tropopause-relative coordinates (bottom row).

3 Results

3.1 Time mean structure

Long-term average (2005 – 2021) cross sections of H_2O from MLS, ACE and WACCM are shown in Fig. 3, with results in both geometric and tropopause-relative coordinates. Patterns highlight the moist troposphere, dry stratosphere and strong gradients
150 across the global tropopause. The tropopause-relative calculations highlight local vertical stratification in extratropics compared to 'fuzzy' structure in geometric coordinates. Careful comparison of the WACCM vs. MLS (or ACE) observations shows enhanced WACCM moisture in the extratropical lowermost stratosphere, and this is quantified in the (WACCM-MLS/MLS) fractional differences shown in Fig. 4. Compared with MLS, WACCM H_2O is more than 300% higher in polar regions and more than 200% higher in subtropical environments in the lower stratosphere of both hemispheres. Such moist biases in the LMS
155 are a common problem for global models, as highlighted in (Charlesworth et al., 2023). We note that this biased H_2O behavior is not simply due to circulation or temperature biases in WACCM, as our simulations use specified dynamics calculations with observed meteorological fields.

3.2 Seasonal ExTL behavior

Seasonal averages in zonal mean tropopause-relative H_2O concentration and atmospheric temperature as observed by MLS are
160 shown in Fig. 5. The tropopause acts as a transport barrier in the extratropics, where there is a sharp gradient in all seasons and in both hemispheres. In the deep tropics, tropopause temperatures vary from ∼192 K in December, January, and February
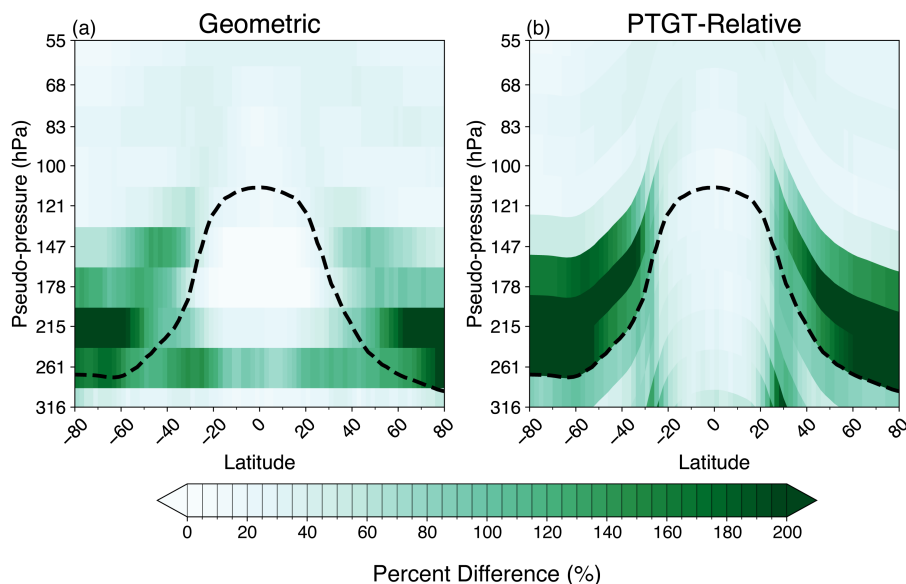
Figure 4. Time average H_2O differences between WACCM and MLS. Results are calculated as fractional (WACCM-MLS/MLS) values.

(DJF) to more than 196 K in June, July, and August (JJA). This seasonal pattern is reflected with in-phase H_2O concentrations at the tropical tropopause (low H_2O during DJF), and this seasonal minimum subsequently propagates upwards in the tropics and spreads in latitude in the lower stratosphere over most of the globe, demonstrating the well-known "tape recorder" signal
165 (Mote et al., 1996). The meridional transport of air via the shallow branch of the BDC is evident in the dry layers extending along isentropic layers to higher latitudes in MAM and all the way to the North Pole in JJA. Notably, this seasonally-varying dry layer does not extend all the way down to the tropopause in the extratropics but stays above ∼215 hPa in the pseudo-pressure coordinates. Air in between this dry layer and the extratropical tropopause is wetter and is a signature of the ExTL. The summer hemisphere ExTL is particularly enhanced relative to the background stratosphere.

170   The hemisphere-averaged annual cycle of lower stratospheric MLS water vapor concentrations in tropopause-following coordinates for both hemispheres is shown in Figs. 6a and c. These data represent area-weighted latitudinal and zonal averages polewards of 20° latitude, as described in Sect. 2.4, and are intended to represent mean hemispheric behaviors. As expected, there are strong vertical gradients across the tropopause. In both the Northern Hemisphere (NH) and Southern Hemisphere (SH) there is a clear annual cycle in upper tropospheric water vapor concentrations which peaks in hemispheric summer (labeled
175 'B' in Figs. 6a and c), extending to the first layer above the tropopause (and weakly to the second layer). In the NH, water vapor concentration peaks at ∼16 ppmv in August in the first layer above the tropopause (∼1.25 km), while there is a peak of ∼7 ppmv in October that occurs ∼2.5 km above the tropopause. There is a similar summertime maximum in the SH for these lowest two stratospheric layers but with smaller amplitude. The dry layer associated with air originating near the tropical tropopause can be seen in Figs. 6a and c in both hemispheres (labeled 'A' in Figs. 6a and 6c), occurring ∼3 – 4 km above
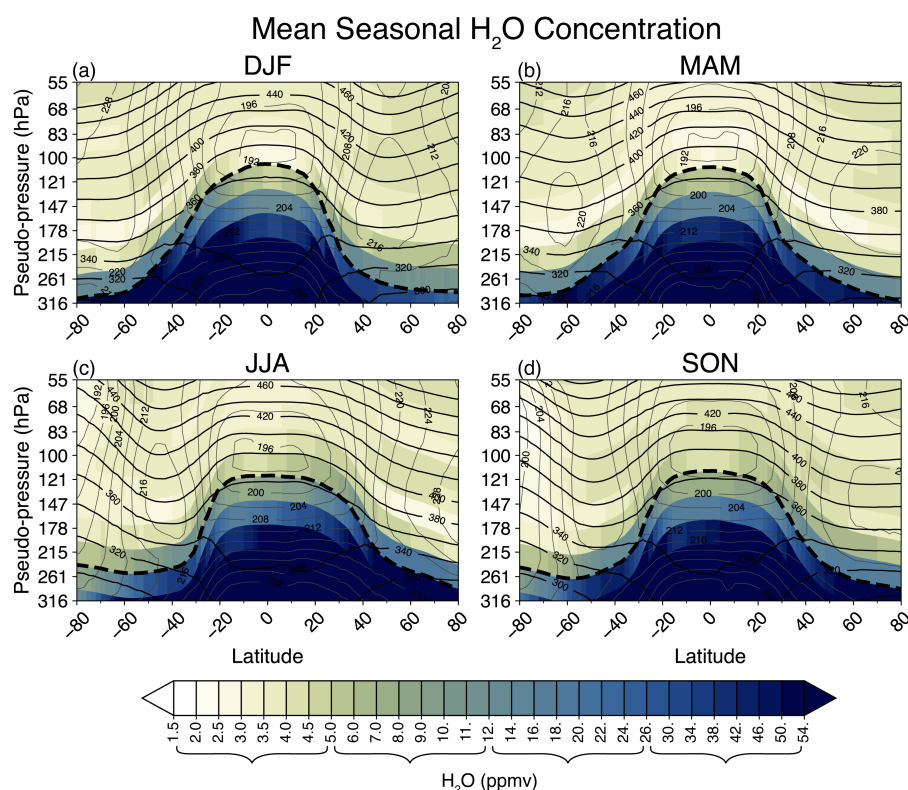
8

Figure 5. Zonally averaged cross sections of MLS H_2O data in tropopause-relative coordinates for (a) DJF, (b) MAM, (c) JJA, (d) SON. Color shading denotes the average MLS H_2O concentration, gray contours indicate temperature as observed by MLS, and black contours denote isentropes. The thick, dashed line is the average PTGT height for each season, calculated from MERRA-2 data.

180   the tropopause in February – August. This distinct seasonal cycle helps define the overworld influence on the water vapor concentrations in the extratropics. It follows that the height of this layer can be used as an upper boundary when defining the ExTL, providing a physically based definition to a layer that fluctuates in both space and time. Although not shown here, similar LMS H_2O seasonal cycles are observed in ACE data, but with limited resolution resulting from the 3-month temporal sampling.

185   Corresponding extratropical LMS seasonal variations for WACCM are shown in Figs. 6b and d. In WACCM, the ExTL has higher H_2O concentrations than MLS and extends $\sim 1 - 2$ km deeper into the stratosphere in both hemispheres, consistent with the time average biases seen in Fig. 4. Hence, the time average WACCM LMS H_2O biases are reflected in a thicker seasonally-evolving ExTL.

         One further minor feature identified in the SH statistics in Figs. 6c and d is a minimum in H_2O in the SH during August

190   – October, $\sim 5 - 7$ km above the tropopause (i.e. geometric altitudes near $15 - 17$ km) (labeled 'C' in Figs. 6c and d). The
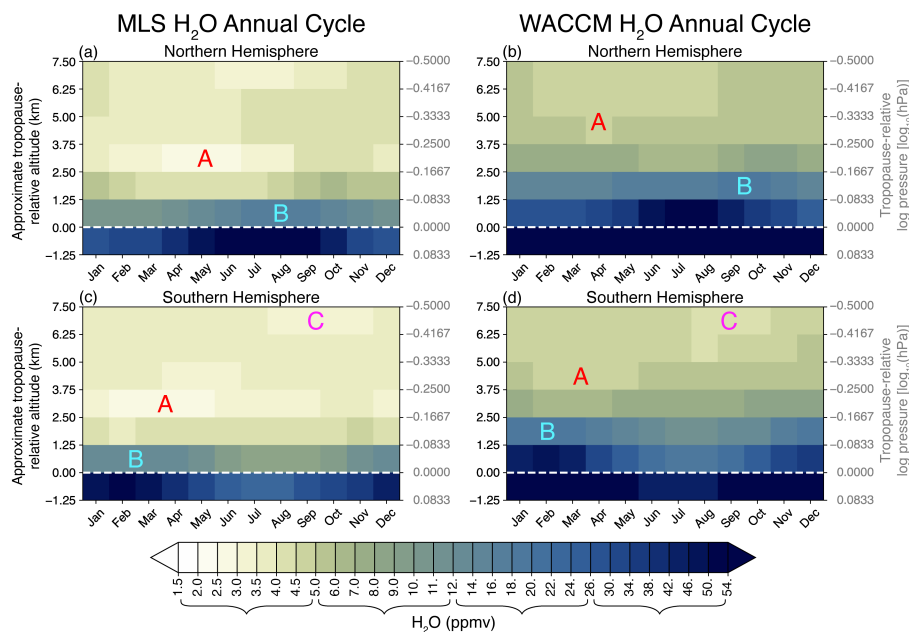
Figure 6. Average annual cycle of area-averaged H_2O concentrations in tropopause-relative coordinates for NH (top) and SH (bottom), showing results from MLS data (left) and WACCM simulation (right). The white horizontal dashed lines denote the tropopause level. The ordinate axis is tropopause-relative altitude. Letters denote specific features related to: (A) seasonal minimum due to overworld transport from tropics, (B) seasonal ExTL maximum tied to summer tropopause, and (C) minimum linked to Antarctic winter dehydration.

altitude and timing of this feature suggest a relation to seasonal dehydration in the Antarctic polar vortex, where effects can spread outside the polar vortex in springtime (e.g., Rosenlof et al., 1997) and may be reflected in hemispheric mean H_2O.

3.3 Interannual Variability

To assess interannual variability and structure, the average monthly seasonal cycle is removed from the MLS time series to create deseasonalized anomalies, with time series for both hemispheres shown in Fig. 7. There is a distinct separation of patterns in the vertical structure occurring around ∼2.5 km above the tropopause in both hemispheres. Above 2.5 km tropopause-relative altitude there are interannual anomalies that are coherent between hemispheres. This variability is closely tied to overworld transport from the tropical tropopause source region, such that air is transported poleward into the extratropical LMS with a time scale of ∼2 − 4 months (e.g., Randel et al., 2024). In the ExTL below 2.5 km tropopause-relative altitude, the interannual patterns are different from above and variability is dominated by an apparent long-term decreasing trend in both hemispheres. This trend is further investigated in Sect. 3.4.

A complementary perspective of the NH and SH anomalies in MLS data at several vertical levels is shown in the time series in Fig. 8. These show time series of overlaid NH and SH data to highlight correlated variability. Strong correlation (r=0.70) is
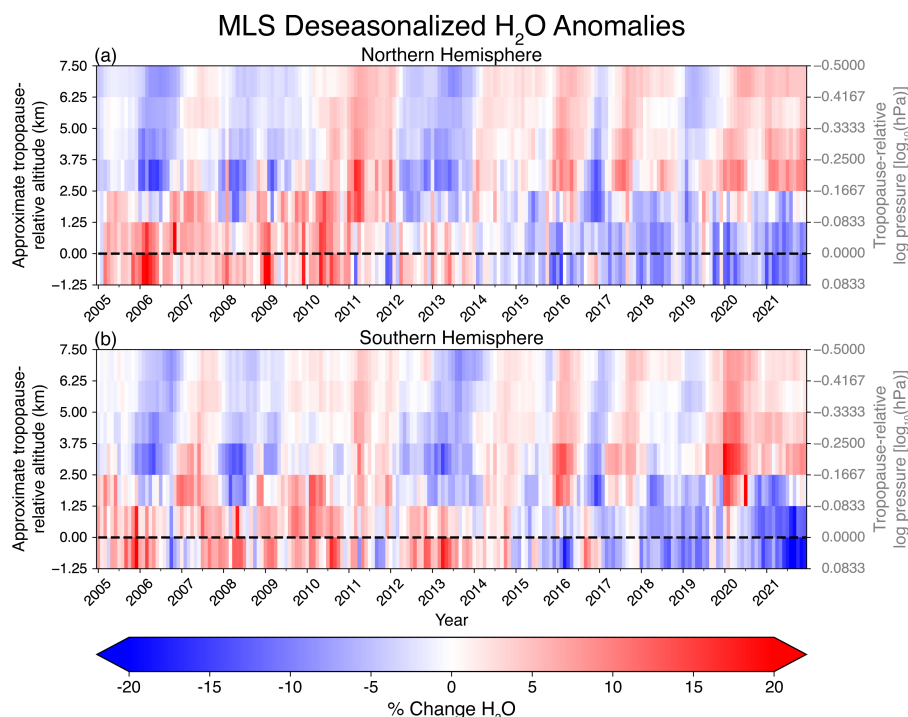
Figure 7. Time series of deseasonalized ExTL area-averaged MLS anomalies in tropopause-relative coordinates for (a) the NH and (b) the SH. Results at each level are expressed in percent deviations from the respective time mean background values.

found at the 3rd level (> 2.5 km above the tropopause), with somewhat weaker correlation (r=0.41) over the 1.2 – 2.5 km layer.

205 The first layer (0 – 1.25 km, within the ExTL) has weak interhemispheric correlation, aside from the strong trends.

Figure 9 provides additional evidence regarding the origin and transport of extratropical overworld anomalies, showing spatial correlations between deseasonalized and detrended water vapor anomalies to a reference point located near the tropical tropopause (83 hPa), with results in both geometric and tropopause-relative coordinates. At zero-time lag there are positive correlations centered in the tropics and extending poleward in a hemispherically symmetric pattern. The tropopause-relative

210 calculations show strong correlations extending downward through the tropical upper troposphere, but this is an artifact of the tropopause-relative coordinates that is not observed in geometric coordinates. At a two-month time lag, the regions of highest correlations spread upward and further poleward in both coordinate systems. The tropopause-relative analysis shows higher extratropical correlations (above 0.6) and more vertically confined branches of positive correlations in the extratropical and polar regions, with the highest correlations occurring a few kms (∼100 hPa) above the tropopause. This is collocated with the

215 dry layer of tropical origin shown in Figs. 5 and 6a-b, and quantifies the vertical profile of overworld transport from the tropics that defines the effective top of the ExTL.

The observed distinction between overworld and ExTL , as identified by their vertical structure and temporal behavior, raises the question of whether similar behavior occurs for other trace gases. Identical to the analysis conducted for Fig. 7,
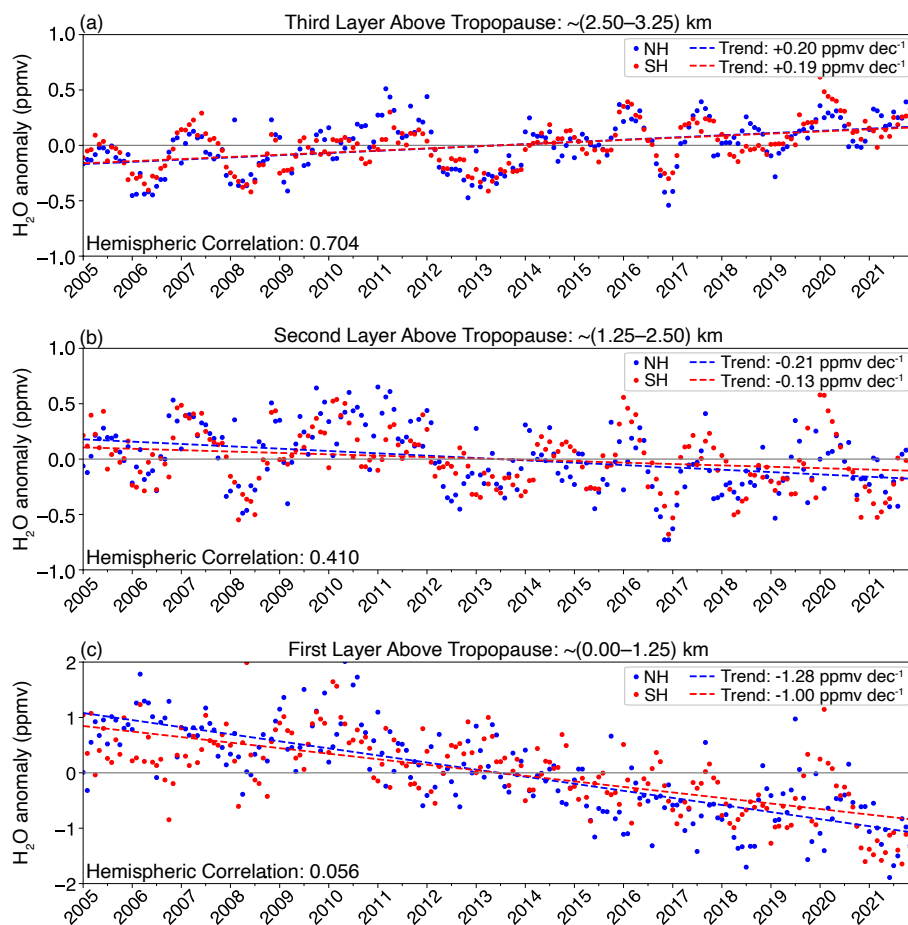
Figure 8. Time series of deseasonalized, tropopause-relative MLS anomalies in the three layers close to the tropopause (bottom to top). NH points are shown in blue, SH points in red, and the trend for each hemisphere is shown as a dashed line in the associated color. The correlation between hemispheres in the detrended time series is given in the bottom left corner of each panel.

deseasonalized ozone anomalies from MLS are shown in Fig. 10. In contrast to the results, there is a coherent vertical structure

220 in each hemisphere in the ozone anomalies that extends from the overworld down to across the tropopause, with no evidence of discontinuity across the ExTL (although the background amounts of ozone changes significantly). Additionally, there is little correlation in the ozone anomalies between the NH and SH, because the main controlling processes (downward transport by the extratropical BDC) is mostly independent between hemispheres. The different behavior for is of course due to the large reservoir of below the tropopause, together with the source of overworld variability in the tropics, distinct from ozone.

225 For comparison with MLS, we also examine deseasonalized water vapor anomalies in ACE and WACCM in Fig. 11. The broad, hemispherically coherent interannual variability seen in MLS above ~2.5 km tropopause-relative altitude is also present in the ACE and WACCM datasets (Figs. 11a-b). ACE reproduces the timing and vertical extent of anomalies seen in MLS but
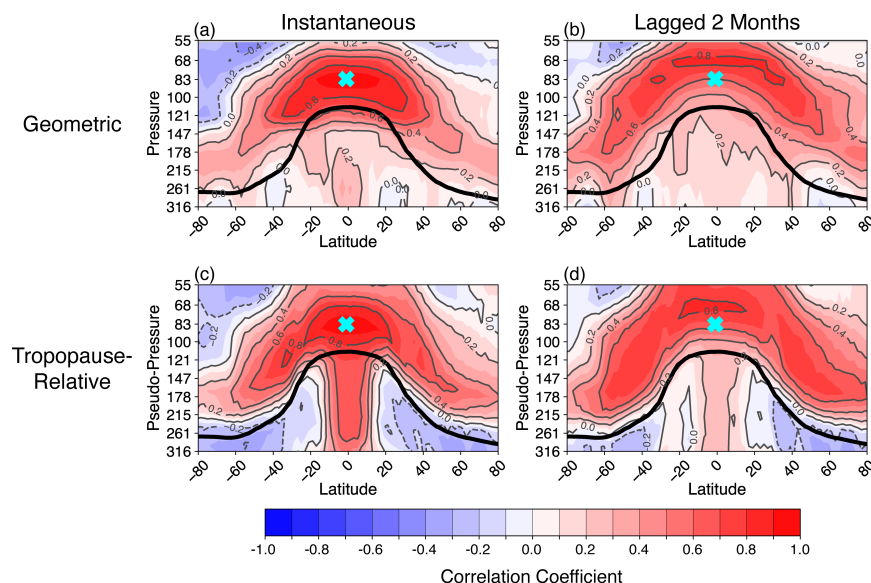
Figure 9. Correlation of deseasonalized MLS water vapor anomalies at each point with the anomaly near the tropical tropopause (teal X; 83 hPa). Correlations are shown in both (top) tropopause-relative and (bottom) geometric coordinate systems at (left) zero-time lag and (right) a two-month time lag.

with greater noise and reduced amplitude, likely related to the latitudinally-varying sampling across seasons. Despite this limitation, the sign and phase of anomalies generally match MLS, supporting consistency between observational datasets.

230 WACCM also matches the overall structure and phase of the overworld anomalies seen in MLS, which is expected due to the prescribed tropical tropopause temperatures used in the specified dynamics run. However, the magnitude of the WACCM variability is substantially larger than MLS, perhaps due to the vertical smearing (~ 3 km) inherent in the MLS data. While the overworld variations are consistent among MLS, ACE and WACCM, the ExTL variations are quite different and neither ACE nor WACCM displays the negative trend observed from MLS in the ExTL layer (Fig. 8c). These comparisons are explored

235 further in Sect. 4.

The vertical variation of the correlation between water vapor anomalies in the NH and SH in each dataset is explored in Fig. 12. The hemispheric correlations in MLS, ACE, and WACCM exhibit a similar vertical structure, with a minimum in the first or second layer above the tropopause, and a maximum that occurs around $4-5$ km above the tropopause. Throughout the vertical profile, hemispheric correlation in ACE is consistently $0.1-0.3$ smaller than MLS. This is likely a reflection of the sparser

240 sampling of the ACE dataset. Comparisons of seasonal means between hemispheres can remain sensitive to the latitudinal distribution of contributing profiles, thereby adding additional sources of variability and reducing the correlation coefficient between hemispheres. The hemispheric correlation in WACCM above 5 km tropopause-relative altitude is nearly identical to MLS, which is expected due to specified dynamics and prescribed tropopause temperatures in the model accurately reflecting stratospheric overworld behavior. Below 5 km tropopause-relative altitude, however, the values of the correlation coefficients
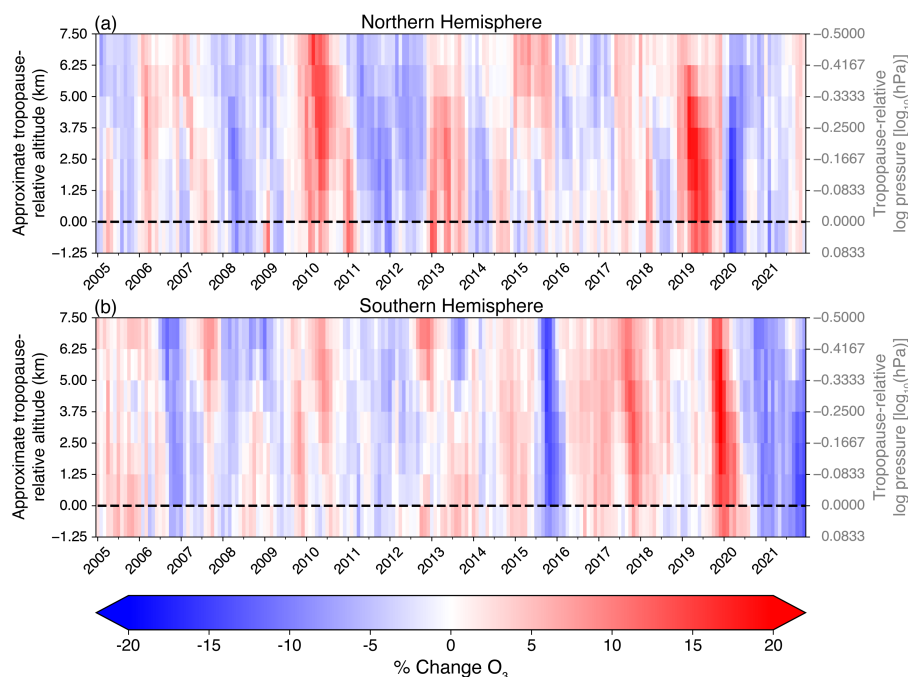
Figure 10. Time series of deseasonalized ExTL area-averaged MLS ozone anomalies for (a) the NH and (b) the SH. Results at each level are expressed in percent deviations from the respective time mean background values.

245 in WACCM are systematically smaller than MLS. This behavior may be a signature of the moist LMS bias and deeper extent of the ExTL in WACCM (e.g., Fig. 6).

 The commonality of higher hemispheric correlation above 4 km tropopause-relative altitude in all three datasets demonstrates that hemispheric symmetry is a robust signature of the stratospheric overworld, resulting from a common stratospheric entry point and similar transport times of the lower branch of the BDC (e.g., Garny et al., 2024; Randel et al., 2024). In diagnosing

250 the vertical structure of the lower stratosphere, hemispheric symmetry and correlation can provide a physical indicator of the separation between the stratospheric overworld, the ExTL, and the hybrid region in between (Fig. 12).

3.4 Trends and other sources of variability in the ExTL

The dominant variability in the ExTL in MLS data is a downward trend (Fig. 8c). However, this trend is not evident in either ACE observations or WACCM simulation (Fig. 11). Here we examine large-scale variability and trends in the global data sets

255 to identify coherent structures and systematically evaluate trends. We conduct a standard multivariate linear regression to the time series at each point and include terms representing a linear trend, ENSO, and the QBO (using two orthogonal time series) to isolate their respective contributions to observed variability (e.g., Godin-Beekmann et al., 2022):
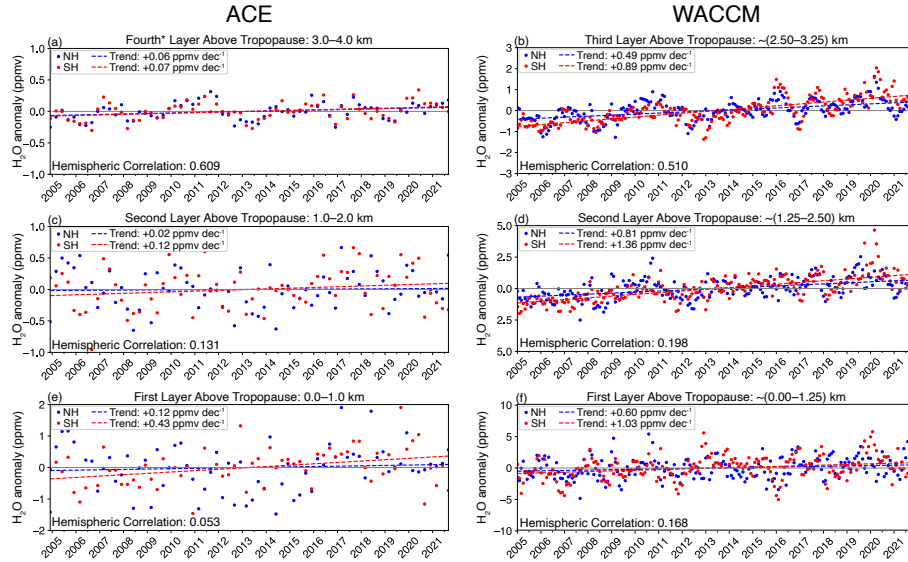
Figure 11. Time series of deseasonalized, tropopause-relative anomalies in three layers close to the tropopause (bottom to top) for ACE observations (left) and WACCM simulation (right). The format is the same as the MLS results in Fig. 8, but note the different scales for WACCM compared to MLS and ACE.

$$y(t) = \beta_0 + \beta_1 t + \beta_2 ENSO(t) + \beta_3 QBO_1(t) + \beta_4 QBO_2(t) + \varepsilon(t) \tag{1}$$

where $\beta_1 t$ represents the trend term and $\varepsilon(t)$ is the residual. The ENSO and QBO proxies are taken from the NOAA Physical
260   Sciences Laboratory Multivariate ENSO Index (MEI) and the NASA Goddard Space Flight Center QBO datasets, respectively.
Results are calculated for both geometric and tropopause-relative coordinates.

Results of the trend calculations are shown for all three data sets in Fig. 13. Trends in the overworld are generally positive in
all data, reflecting a slight increase in cold point temperature over the data record 2005 – 2021. Similar positive stratospheric
trends over this time period have been shown in Sheese et al. (2025), Tao et al. (2023), Konopka et al. (2022), and Yu et al.
265   (2022). In contrast, trends in the troposphere and ExTL of both hemispheres are very different among the data. MLS exhibits
negative trends in the global upper troposphere and ExTL regions, with patterns that generally follow the global tropopause
structure. The trends are slightly more negative in tropopause-relative coordinates, reflecting the slight rise of the tropopause
over this period (e.g., Ladstädter et al., 2025; Meng et al., 2021), which acts to reduce values in the tropopause region, all else
being equal. However, these negative trends derived from MLS data are not evident in either ACE observations or WACCM
270   simulation, and these differences question the reality of the MLS trend results, as discussed further below.

Regression fits for ENSO variability are shown in Fig. 14. In general, is expected to follow temperture changes throughout
the troposphere (from the Clausius-Clapeyron relationship), so that positive ENSO regression patterns are expected in the
troposphere following the well-known positive zonal mean temperature changes for ENSO (e.g., Li et al., 2024; Johnston
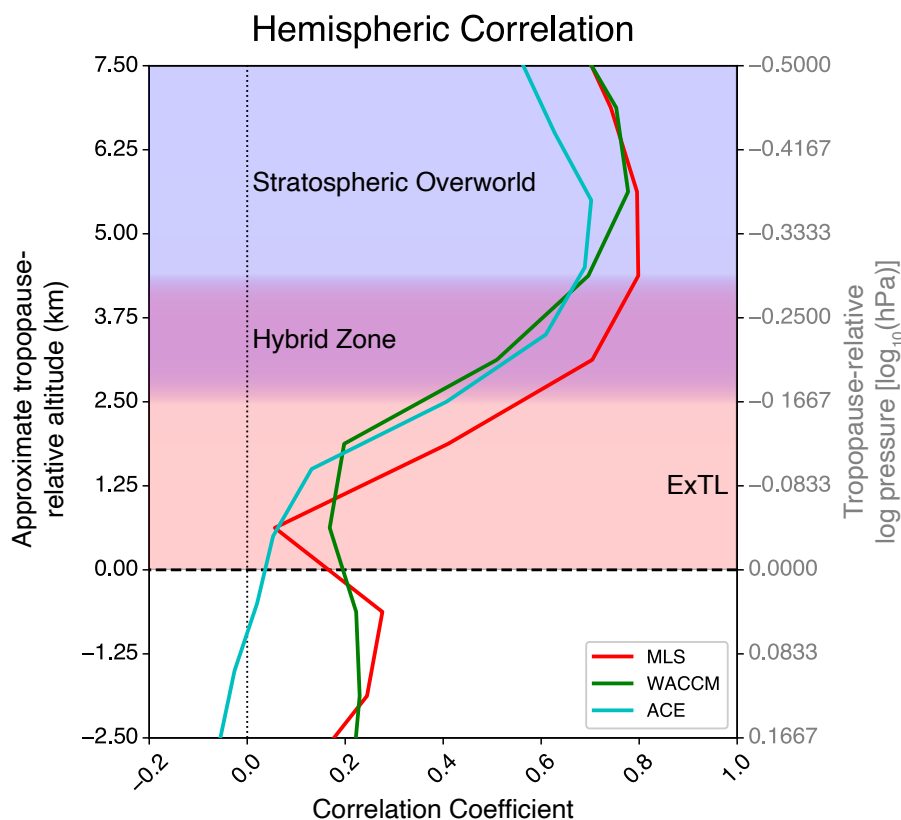
15

Figure 12. Correlation coefficient between NH and SH extratropical detrended and deseasonalized anomalies on tropopause-relative levels for MLS (red), WACCM (green), and ACE (teal). Subjectively identified regions are depicted by background shading for the ExTL (red), the overworld (blue), and a hybrid zone (purple).

et al., 2022). This positive ENSO signal is observed in MLS, ACE and WACCM geometric coordinate results (top row in
275 Fig. 14), with patterns covering the tropical upper troposphere and extending across the tropopause to higher latitudes in both hemispheres. Hence, ENSO is a significant component of ExTL variability. However, the broad-scale ENSO signature is much less coherent (and insignificant) in tropopause-relative coordinates (bottom row of Fig. 14), because the ENSO-related changes in tropopause height confuse the signal in the tropics.

The global QBO1 pattern in MLS data is shown in Fig. 15. The QBO1 index is negatively correlated with tropical cold
280 point temperature (e.g., Randel et al., 2015) and this produces a negative correlation with in the tropics and global lower stratosphere (i.e. overworld). Results in tropopause-relative coordinates show sharper and more vertically stratified patterns that delineate overworld influence and ExTL structure. QBO1 patterns in the troposphere in Fig. 15b (negative values over the equator and positive below the tropopause in extratropics) reflect the influence of the QBO on tropopause height, and are artifacts of the coordinate system. Similar QBO regression results are found in ACE and WACCM data and are not shown here.
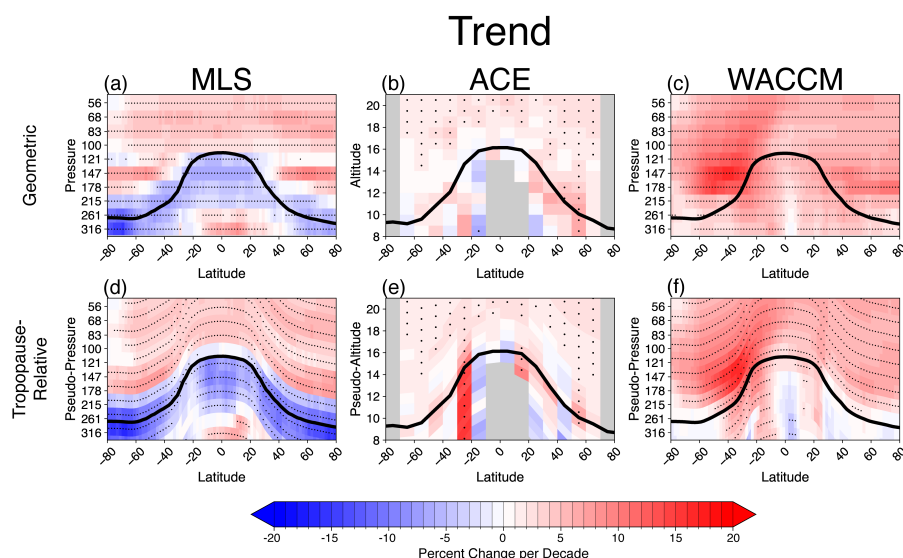285 QBO2 regression coefficients have little impact on the CPT and hence have less impact on (not shown here).

16

Figure 13. Latitude-height sections of trends for MLS data (left), ACE data (middle) and WACCM simulation (right), calculated in geometric coordinates (top row) and tropopause-relative coordinates (bottom). Results are shown in %/decade, calculated with respect to the respective long-term background values. Stippling denotes 95% statistically significant values.
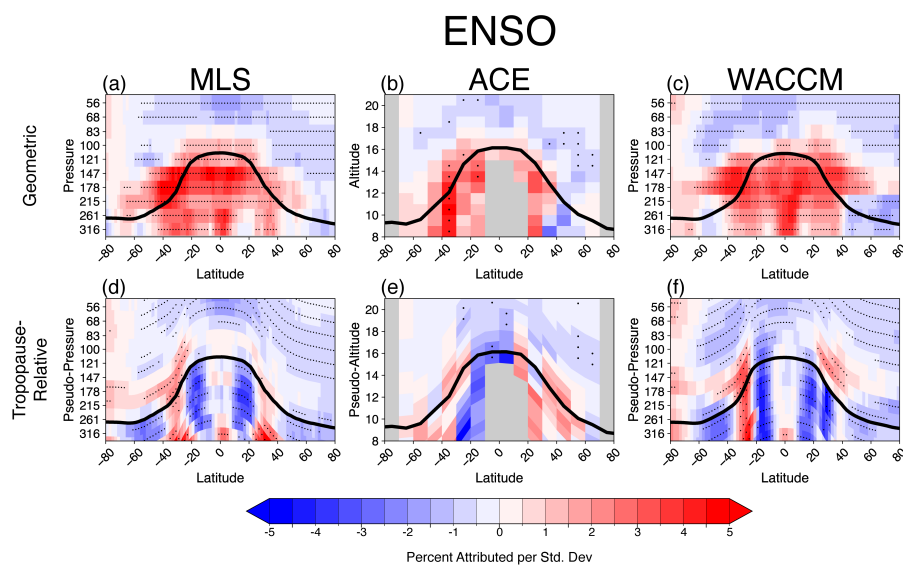

Figure 14. Latitude-height sections of ENSO regression fit to for MLS data (left), ACE data (middle) and WACCM simulation (right), calculated in geometric coordinates (top row) and tropopause-relative coordinates (bottom). Results are shown in %/normalized ENSO index, calculated with respect to the respective long-term background values.
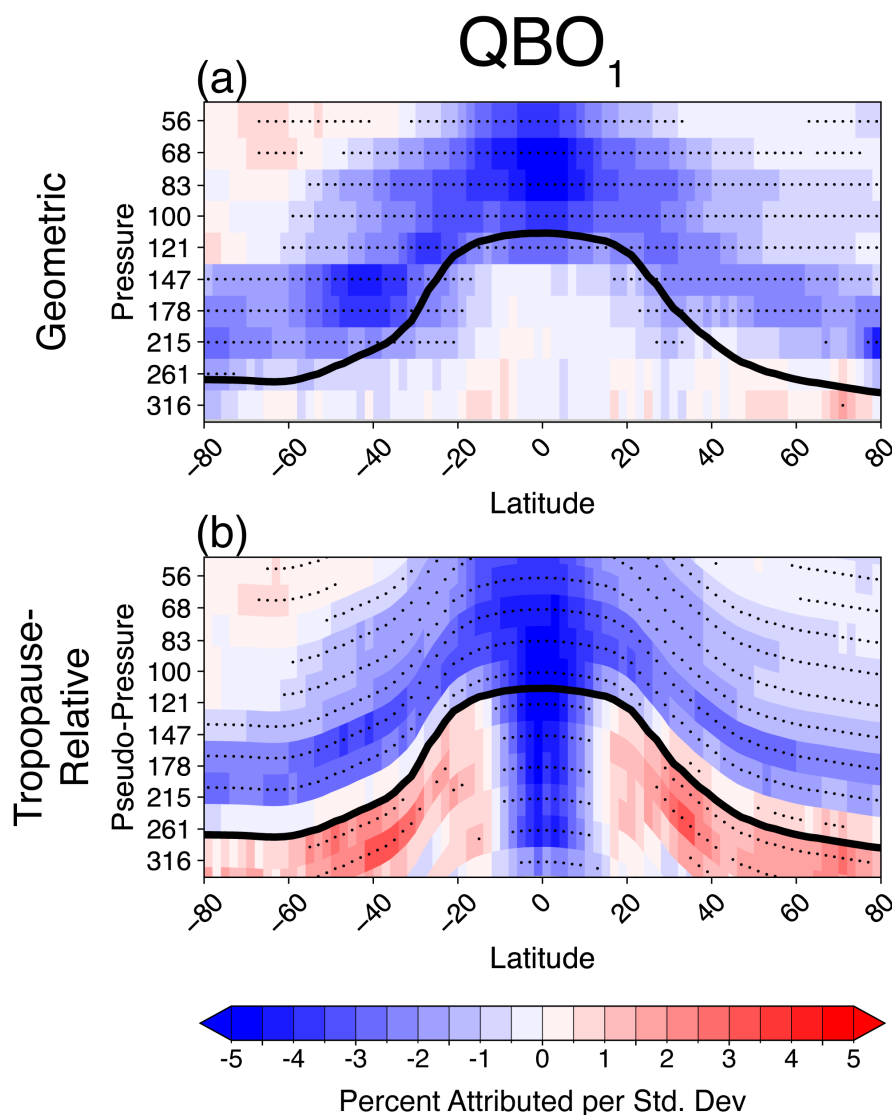
Figure 15. Latitude-height sections of QBO1 regression fit to for MLS data, calculated in geometric coordinates (top) and tropopause-relative coordinates (bottom). Results are shown in %/normalized QBO1 index, calculated with respect to the respective long-term background values.

4 Summary and discussion

This work has examined the variability and vertical structure of in the extratropical lower stratosphere, using geometric and tropopause-relative coordinate analysis of monthly mean satellite data and WACCM global model simulations. The use of tropopause-relative coordinates reduces seasonal and interannual variance in the ExTL regions and sharpens the geophysical
290 structure evident in the data. However, tropopause-relative coordinates are not as useful in the deep tropics, as they introduce

additional variance in the upper troposphere and can confuse interpretation of results (e.g. the ENSO regressions in Fig. 14). The ExTL (transition region in extratropics) is identified in the observed seasonal and interannual anomaly patterns to span the first 2.5 km above the tropopause; we note that this result should be interpreted considering the approximate 3 km vertical resolution of the MLS and ACE satellite retrievals. However, this value is consistent with the depth of the ExTL diagnosed

295 from aircraft and balloon measurements in midlatitudes (e.g., Gettelman et al., 2011; Pan et al., 2004; Hoor et al., 2002). variability above the ExTL (in the stratospheric overworld) is correlated between hemispheres, identifying a source region for both hemispheres near the tropical tropopause (Fig. 12). In the ExTL and below, variability is tied to tropospheric and is uncorrelated between the NH and SH. While ENSO is one source of global-scale variability that extends from the tropical upper troposphere across the tropopause into the LMS (Fig. 14 in geometric coordinates), more generally the ExTL is independent

300 between the NH and SH. As a note, LMS ozone interannual variability is very different from , with little coherence between hemispheres and no change in behavior of anomalies across the ExTL.

The WACCM simulations using observed meteorological fields show much of the same LMS structure and variability as the satellite observations, although direct comparisons highlight a strong positive model bias in the LMS. This behavior was noted in Charlesworth et al. (2023) and shown to be a feature of other global models (e.g. CMIP6). Charlesworth et al. (2023)

305 diagnose a cause of overly diffusive transport as one source of this model bias, which ends up impacting LMS temperatures and global circulations. The wet LMS bias in WACCM is found in seasonal (Fig. 6) and interannual anomalies (Fig. 11f) across the ExTL, and the ExTL is approximately 1-2 km deeper in WACCM compared to satellite data (Fig. 12).

MLS observations show strong negative trends in the global upper troposphere that extend across the tropopause and dominate variability in the ExTL (e.g. Fig. 8c). The global trend patterns (Fig. 13a) approximately follow the region with background

310 values on the order of 300 ppmv in the troposphere extending down to ∼20 ppmv in the ExTL. These trends are evident in geometric coordinates and are slightly enhanced in tropopause-relative coordinates due to the long-term rise of the extratropical tropopause. The negative global-scale trends in MLS data are not evident in ACE observations or in our specified dynamics WACCM simulations, and they are not expected due to the generally increasing background tropospheric temperatures over 2005 − 2021 (as quantified by the WACCM specified dynamics calculations). The MLS decreases in the tropical upper tropo-

315 sphere seen in Fig. 13 also disagree with other infrared and microwave satellite observations, which show consistent specific humidity increases in this region over the recent decades (e.g., John et al., 2025; Allan et al., 2022). Likewise, results for ERA5 reanalysis show moistening of the tropical upper troposphere since 2000 (e.g., Li et al., 2024; Allan et al., 2022). As a result, we view the negative trends with a skeptical eye as a potential retrieval artifact of the MLS data that should be further investigated.

Data availability. MLS (Lambert et al., 2020; Schwartz, 2021), MERRA-2 (Global Modeling and Assimilation Office (GMAO), 2015), and

320 ACE (Bernath et al., 2025) are publicly available datsets. CESM2/WACCM6 is an open-source community model, which was developed with support primarily from the National Science Founation. WACCM6 source code can be downloaded at https://www.cesm.ucar.edu/models/cesm2/download.

References

Allan, R. P., Willett, K. M., John, V. O., and Trent, T.: Global Changes in Water Vapor 1979–2020, J. Geophys. Res. Atmos., 127, e2022JD036 728, https://doi.org/https://doi.org/10.1029/2022JD036728, e2022JD036728 2022JD036728, 2022.

335 Banerjee, A., Chiodo, G., Previdi, M., Ponater, M., Conley, A. J., and Polvani, L. M.: Stratospheric water vapor: an important climate feedback, Clim. Dyn., 53, 1697–1710, https://doi.org/10.1007/s00382-019-04721-4, 2019.

Bernath, P. F., McElroy, C. T., Abrams, M. C., Boone, C. D., Butler, M., Camy-Peyret, C., Carleer, M., Clerbaux, C., Coheur, P.-F., Colin, R., DeCola, P., DeMazière, M., Drummond, J. R., Dufour, D., Evans, W. F. J., Fast, H., Fussen, D., Gilbert, K., Jennings, D. E., Llewellyn, E. J., Lowe, R. P., Mahieu, E., McConnell, J. C., McHugh, M., McLeod, S. D., Michaud, R., Midwinter, C., Nassar, R., Nichitiu, F., Nowlan, C., Rinsland, C. P., Rochon, Y. J., Rowlands, N., Semeniuk, K., Simon, P., Skelton, R., Sloan, J. J., Soucy, M.-A., Strong,

340 K., Tremblay, P., Turnbull, D., Walker, K. A., Walkty, I., Wardle, D. A., Wehrle, V., Zander, R., and Zou, J.: Atmospheric Chemistry Experiment (ACE): Mission overview, Geophys. Res. Lett., 32, https://doi.org/https://doi.org/10.1029/2005GL022386, 2005.

Bernath, P. F., Boone, C. D., Lecours, M. J., Crouse, J., Steffen, J., and Schmidt, M.: Global Satellite-Based Atmospheric Profiles from Atmospheric Chemistry Experiment SciSat Level 2 Processed Data, v5.2, 2004-2024, https://doi.org/10.20383/103.01245, 2025.

Bland, J., Gray, S., Methven, J., and Forbes, R.: Characterising extratropical near-tropopause analysis humidity biases and their radiative

345 effects on temperature forecasts, Q. J. R. Meteorol. Soc., 147, 3878–3898, https://doi.org/https://doi.org/10.1002/qj.4150, 2021.

Boothe, A. C. and Homeyer, C. R.: Global large-scale stratosphere–troposphere exchange in modern reanalyses, Atmos. Chem. Phys., 17, 5537–5559, https://doi.org/10.5194/acp-17-5537-2017, 2017.

Butchart, N.: The Brewer-Dobson circulation, Rev. Geophys., 52, 157–184, https://doi.org/https://doi.org/10.1002/2013RG000448, 2014.

Chang, K.-W., Bowman, K. P., and Rapp, A. D.: Transport and Confinement of Plumes From Tropopause-Overshooting Con-

350 vection Over the Contiguous United States During the Warm Season, J. Geophys. Res. Atmos., 128, e2022JD037 020, https://doi.org/https://doi.org/10.1029/2022JD037020, e2022JD037020 2022JD037020, 2023.

Charlesworth, E., Plöger, F., Birner, T., Baikhadzhaev, R., Abalos, M., Abraham, N. L., Akiyoshi, H., Bekki, S., Dennison, F., Jöckel, P., Keeble, J., Kinnison, D., Morgenstern, O., Plummer, D., Rozanov, E., Strode, S., Zeng, G., Egorova, T., and Riese, M.: Stratospheric water vapor affecting atmospheric circulation, Nat. Commun., 14, 3925, https://doi.org/10.1038/s41467-023-39559-2, 2023.

355 Danabasoglu, G., Lamarque, J.-F., Bacmeister, J., Bailey, D. A., DuVivier, A. K., Edwards, J., Emmons, L. K., Fasullo, J., Garcia, R., Gettelman, A., Hannay, C., Holland, M. M., Large, W. G., Lauritzen, P. H., Lawrence, D. M., Lenaerts, J. T. M., Lindsay, K., Lipscomb, W. H., Mills, M. J., Neale, R., Oleson, K. W., Otto-Bliesner, B., Phillips, A. S., Sacks, W., Tilmes, S., van Kampenhout, L., Vertenstein, M., Bertini, A., Dennis, J., Deser, C., Fischer, C., Fox-Kemper, B., Kay, J. E., Kinnison, D., Kushner, P. J., Larson, V. E., Long, M. C., Mickelson, S., Moore, J. K., Nienhouse, E., Polvani, L., Rasch, P. J., and Strand, W. G.: The Community Earth System Model Version

360 2 (CESM2), J. Adv. Model. Earth Syst., 12, e2019MS001 916, https://doi.org/https://doi.org/10.1029/2019MS001916, e2019MS001916 2019MS001916, 2020.

Dessler, A. E., Schoeberl, M. R., Wang, T., Davis, S. M., and Rosenlof, K. H.: Stratospheric water vapor feedback, PNAS, 110, 18 087– 18 091, https://doi.org/10.1073/pnas.1310344110, 2013.

Forster, P. M. d. F. and Shine, K. P.: Assessing the climate impact of trends in stratospheric water vapor, Geophys. Res. Lett., 29, 10–1–10–4,

365 https://doi.org/https://doi.org/10.1029/2001GL013909, 2002.

Garny, H., Ploeger, F., Abalos, M., Bönisch, H., Castillo, A. E., von Clarmann, T., Diallo, M., Engel, A., Laube, J. C., Linz, M., Neu, J. L., Podglajen, A., Ray, E., Rivoire, L., Saunders, L. N., Stiller, G., Voet, F., Wagenhäuser, T., and Walker, K. A.:

Age of Stratospheric Air: Progress on Processes, Observations, and Long-Term Trends, Rev. Geophys., 62, e2023RG000 832, https://doi.org/https://doi.org/10.1029/2023RG000832, e2023RG000832 2023RG000832, 2024.

370 Gelaro, R., McCarty, W., Suárez, M. J., Todling, R., Molod, A., Molod, A., Takacs, L., Randles, C. A., Darmenov, A., Bosilovich, M. G., Reichle, R., Wargan, K., Coy, L., Cullather, R., Draper, C., Akella, S., Buchard, V., Conaty, A., Da Silva, A. M., Gu, W., Kim, G.-K., Koster, R., Lucchesi, R., Merkova, D., Nielsen, J. E., Partyka, G., Pawson, S., Putnam, W., Rienecker, M., Schubert, S. D., Sienkiewicz, M., and Zhao, B.: The Modern-Era Retrospective Analysis for Research and Applications, Version 2 (MERRA-2), J. Clim., 30, 5419–5454, https://doi.org/10.1175/JCLI-D-16-0758.1, 2017.

375 Gettelman, A., Hoor, P., Pan, L. L., Randel, W. J., Hegglin, M. I., and Birner, T.: The extratropical upper troposphere and lower stratosphere, Rev. Geophys., 49, RG3003, https://doi.org/10.1029/2011RG000355, 2011.

Gettelman, A., Mills, M. J., Kinnison, D. E., Garcia, R. R., Smith, A. K., Marsh, D. R., Tilmes, S., Vitt, F., Bardeen, C. G., McInerny, J., Liu, H.-L., Solomon, S. C., Polvani, L. M., Emmons, L. K., Lamarque, J.-F., Richter, J. H., Glanville, A. S., Bacmeister, J. T., Phillips, A. S., Neale, R. B., Simpson, I. R., DuVivier, A. K., Hodzic, A., and Randel, W. J.: The Whole Atmosphere Community Climate Model Version

380 6 (WACCM6), J. Geophys. Res. Atmos., 124, 12 380–12 403, https://doi.org/https://doi.org/10.1029/2019JD030943, 2019.

Global Modeling and Assimilation Office (GMAO): MERRA-2 inst3_3d_asm_Nv: 3d, 3-Hourly, Instantaneous, Model-Level, Assimilation, Assimilated Meteorological Fields V5.12.4, https://doi.org/10.5067/WWQSXQ8IVFW8, 2015.

Godin-Beekmann, S., Azouz, N., Sofieva, V. F., Hubert, D., Petropavlovskikh, I., Effertz, P., Ancellet, G., Degenstein, D. A., Zawada, D., Froidevaux, L., Frith, S., Wild, J., Davis, S., Steinbrecht, W., Leblanc, T., Querel, R., Tourpali, K., Damadeo, R., Maillard Barras, E.,

385 Stübi, R., Vigouroux, C., Arosio, C., Nedoluha, G., Boyd, I., Van Malderen, R., Mahieu, E., Smale, D., and Sussmann, R.: Updated trends of the stratospheric ozone vertical distribution in the 60° S–60° N latitude range based on the LOTUS regression model, Atmos. Chem. Phys., 22, 11 657–11 673, https://doi.org/10.5194/acp-22-11657-2022, 2022.

Haynes, P., Scinocca, J., and Greenslade, M.: Formation and maintenance of the extratropical tropopause by baroclinic eddies, Geophys. Res. Lett., 28, 4179–4182, https://doi.org/https://doi.org/10.1029/2001GL013485, 2001.

390 He, R. and Huang, Y.: Muted Radiative Feedback of Stratospheric Water Vapor Found in a Multimodel Assessment, J. Geophys. Res. Atmos., 130, e2025JD043 676, https://doi.org/https://doi.org/10.1029/2025JD043676, e2025JD043676 2025JD043676, 2025.

Holton, J. R., Haynes, P. H., McIntyre, M. E., Douglass, A. R., Rood, R. B., and Pfister, L.: Stratosphere-troposphere exchange, Rev. Geophys., 33, 403–439, https://doi.org/10.1029/95RG02097, 1995.

Homeyer, C. R. and Bowman, K. P.: Rossby Wave Breaking and Transport between the Tropics and Extratropics above the Subtropical Jet,

395 J. Atmos. Sci., 70, 607–626, https://doi.org/10.1175/JAS-D-12-0198.1, 2013.

Homeyer, C. R., Bowman, K. P., Pan, L. L., Atlas, E. L., Gao, R.-S., and Campos, T. L.: Dynamical and chemical characteristics of tropospheric intrusions observed during START08, J. Geophys. Res. Atmos., 116, https://doi.org/https://doi.org/10.1029/2010JD015098, 2011.

Hoor, P., Fischer, H., Lange, L., Lelieveld, J., and Brunner, D.: Seasonal variations of a mixing layer in the lowermost stratosphere as identified

400 by the CO-O3 correlation from in situ measurements, J. Geophys. Res., 107, 4044, https://doi.org/10.1029/2000JD000289, 2002.

Hoskins, B. J.: Towards a PV- view of the general circulation, Tellus B, 43, 27–35, https://doi.org/https://doi.org/10.1034/j.1600-0889.1991.t01-3-00005.x, 1991.

John, V., Shi, L., Chung, E.-S., Stevens, T., Allan, R. P., Buehler, S. A., and Soden, B. J.: Upper tropospheric humidity [in "State of the Climate in 2024"], Bulletin of the American Meteorological Society, 106, S63 – S64, https://doi.org/10.1175/BAMS-D-25-0102.1, 2025.

405　Johnston, B. R., Randel, W. J., and Braun, J. J.: Interannual Variability of Tropospheric Moisture and Temperature and Relationships to
　　　ENSO Using COSMIC-1 GNSS-RO Retrievals, J. Clim., 35, 7109 – 7125, https://doi.org/10.1175/JCLI-D-21-0884.1, 2022.

　　　Konopka, P., Tao, M., Ploeger, F., Hurst, D. F., Santee, M. L., Wright, J. S., and Riese, M.: Stratospheric Moistening After 2000, Geophys.
　　　Res. Lett., 49, e2021GL097 609, https://doi.org/https://doi.org/10.1029/2021GL097609, e2021GL097609 2021GL097609, 2022.

　　　Ladstädter, F., Stocker, M., Scher, S., and Steiner, A. K.: Observed changes in the temperature and height of the globally resolved lapserate
410　tropopause, Atmos. Chem. Phys., 25, 16 053–16 062, https://doi.org/10.5194/acp-25-16053-2025, 2025.

　　　Lambert, A., Read, W., and Livesey, N.: MLS/Aura Level 2 Water Vapor (H2O) Mixing Ratio V005,
　　　https://doi.org/10.5067/Aura/MLS/DATA2508, 2020.

　　　Li, F. and Newman, P.: Stratospheric water vapor feedback and its climate impacts in the coupled atmosphere–ocean Goddard Earth Observ-
　　　ing System Chemistry-Climate Model, Clim. Dyn., 55, 1585–1595, https://doi.org/10.1007/s00382-020-05348-6, 2020.

415　Li, L., Chen, Z., Wang, B., Fan, J., Lu, T., and Lv, K.: Response of upper tropospheric water vapor to global warming and ENSO, Sci. Rep.,
　　　14, 5995, https://doi.org/10.1038/s41598-024-56639-5, 2024.

　　　Lin, S.-J. and Rood, R. B.: Multidimensional Flux-Form Semi-Lagrangian Transport Schemes, Mon. Weather Rev., 124, 2046 – 2070,
　　　https://doi.org/10.1175/1520-0493(1996)124<2046:MFFSLT>2.0.CO;2, 1996.

　　　Liu, Y., Xu, T., and Liu, J.: Characteristics of the seasonal variation of the global tropopause revealed by COSMIC/GPS data, Adv. Space
420　Res., 54, 2274–2285, https://doi.org/https://doi.org/10.1016/j.asr.2014.08.020, 2014.

　　　Livesey, N. J., Read, W. G., Wagner, P. A., Froidevaux, L., Santee, M. L., Schwartz, M. J., Lambert, A., Valle, L. F. M., Pumphrey, H. C.,
　　　Manney, G. L., Fuller, R. A., Jarnot, R. F., Knosp, B. W., and Lay, R. R.: Earth Observing System (EOS) Aura Microwave Limb Sounder
　　　(MLS): Version 5.0x Level 2 and 3 data quality and description document., available online at: https://mls.jpl.nasa.gov/data/v5-0_data_
　　　quality_document.pdf, 2022.

425　Meng, L., Liu, J., Tarasick, D. W., Randel, W. J., Steiner, A. K., Wilhelmsen, H., Wang, L., and Haimberger, L.: Continous rise of the
　　　tropopause in the Northern Hemisphere over 1980–2020, Sci. Adv., 7, eabi8065, https://doi.org/10.1126/sciadv.abi8065, 2021.

　　　Millán, L. F., Hoor, P., Hegglin, M. I., Manney, G. L., Boenisch, H., Jeffery, P., Kunkel, D., Petropavlovskikh, I., Ye, H., Leblanc, T., and
　　　Walker, K.: Exploring ozone variability in the upper troposphere and lower stratosphere using dynamical coordinates, Atmos. Chem.
　　　Phys., 24, 7927–7959, https://doi.org/10.5194/acp-24-7927-2024, 2024.

430　Mote, P. W., Rosenlof, K. H., McIntyre, M. E., Carr, E. S., Gille, J. C., Holton, J. R., Kinnersley, J. S., Pumphrey, H. C., Russell III, J. M., and
　　　Waters, J. W.: An atmospheric tape recorder: The imprint of tropical tropopause temperatures on stratospheric water vapor, J. Geophys.
　　　Res. Atmos., 101, 3989–4006, https://doi.org/https://doi.org/10.1029/95JD03422, 1996.

　　　Olsen, M. A., Douglass, A. R., Newman, P. A., Gille, J. C., Nardi, B., Yudin, V. A., Kinnison, D. E., and Khosravi, R.: HIRDLS
　　　observations and simulation of a lower stratospheric intrusion of tropical air to high latitudes, Geophys. Res. Lett., 35, L21 813,
435　https://doi.org/10.1029/2008GL035514, 2008.

　　　Pan, L. L., Randel, W. J., Gary, B. L., Mahoney, M. J., and Hintsa, E. J.: Definitions and sharpness of the extratropical tropopause: A trace
　　　gas perspective, J. Geophys. Res. Atmos., 109, https://doi.org/10.1029/2004JD004982, 2004.

　　　Pan, L. L., Randel, W. J., Gille, J. C., Hall, W. D., Nardi, B., Massie, S., Yudin, V., Khosravi, R., Konopka, P., and Tarasick, D.: Tropospheric
　　　intrusions associated with the secondary tropopause, J. Geophys. Res. Atmos., 114, https://doi.org/10.1029/2008JD011374, 2009.

440　Pan, L. L., Kinnison, D., Liang, Q., Chin, M., Santee, M. L., Flemming, J., Smith, W. P., Honomichl, S. B., Bresch, J. F., Lait, L. R., Zhu,
　　　Y., Tilmes, S., Colarco, P. R., Warner, J., Vuvan, A., Clerbaux, C., Atlas, E. L., Newman, P. A., Thornberry, T., Randel, W. J., and Toon,

O. B.: A Multimodel Investigation of Asian Summer Monsoon UTLS Transport Over the Western Pacific, J. Geophys. Res. Atmos., 127, e2022JD037 511, https://doi.org/https://doi.org/10.1029/2022JD037511, e2022JD037511 2022JD037511, 2022.

Randel, W. and Park, M.: Diagnosing Observed Stratospheric Water Vapor Relationships to the Cold Point Tropical Tropopause, J. Geophys.
445   Res. Atmos., 124, 7018–7033, https://doi.org/https://doi.org/10.1029/2019JD030648, 2019.

Randel, W. J., Wu, F., and Gaffen, D. J.: Interannual variability of the tropical tropopause derived from radiosonde data and NCEP reanalyses, J. Geophys. Res. Atmos., 105, 15 509–15 523, https://doi.org/https://doi.org/10.1029/2000JD900155, 2000.

Randel, W. J., Seidel, D. J., and Pan, L. L.: Observational characteristics of double tropopauses, J. Geophys. Res., 112, D07 309, https://doi.org/10.1029/2006JD007904, 2007.

450   Randel, W. J., Zhang, K., and Fu, R.: What controls stratospheric water vapor in the NH summer monsoon regions?, J. Geophys. Res. Atmos., 120, 7988–8001, https://doi.org/10.1002/2015JD023622, 2015.

Randel, W. J., Podglajen, A., and Wu, F.: Stratospheric Transit Time Distributions Derived From Satellite Water Vapor Measurements, J. Geophys. Res. Atmos., 129, e2024JD041 595, https://doi.org/https://doi.org/10.1029/2024JD041595, e2024JD041595 2024JD041595, 2024.

455   Rosenlof, K. H., Tuck, A. F., Kelly, K. K., Russell III, J. M., and McCormick, M. P.: Hemispheric asymmetries in water vapor and inferences about transport in the lower stratosphere, J. Geophys. Res. Atmos., 102, 13 213–13 234, https://doi.org/https://doi.org/10.1029/97JD00873, 1997.

Schwartz, M.: MLS/Aura Level 2 Ozone (O3) Mixing Ratio V005, https://doi.org/10.5067/AURA/MLS/DATA2516, 2021.

Schwartz, M. J., Manney, G. L., Hegglin, M. I., Livesey, N. J., Santee, M. L., and Daffer, W. H.: Climatology and variability of trace gases
460   in extratropical double-tropopause regions from MLS, HIRDLS, and ACE-FTS measurements, J. Geophys. Res. Atmos., 120, 843–867, https://doi.org/10.1002/2014JD021964, 2015.

Sheese, P. E., Boone, C. D., and Walker, K. A.: Detecting physically unrealistic outliers in ACE-FTS atmospheric measurements, Atmos. Meas. Tech., 8, 741–750, https://doi.org/10.5194/amt-8-741-2015, 2015.

Sheese, P. E., Walker, K. A., Boone, C. D., and Plummer, D. A.: Quantifying the sources of increasing stratospheric water vapour concentra-
465   tions, Atmos. Chem. Phys., 25, 5199–5213, https://doi.org/10.5194/acp-25-5199-2025, 2025.

Solomon, S., Rosenlof, K. H., Portmann, R. W., Daniell, J. S., Davis, S. M., Sanford, T. J., and Plattner, G.-K.: Contributions of Stratospheric Water Vapor to Decadal Changes in the Rate of Global Warming, Science, 327, 1219–1223, https://doi.org/10.1126/science.1182488, 2010.

Stohl, A., Wernli, H., James, P., Bourqui, M., Forster, C., Liniger, M. A., Seibert, P., and Sprenger, M.: A new perspective of stratosphere-
470   troposphere exchange, Bull. Amer. Meteorol. Soc., 84, 1565–1573, 2003.

Tao, M., Konopka, P., Wright, J. S., Liu, Y., Bian, J., Davis, S. M., Jia, Y., and Ploeger, F.: Multi-decadal variability controls short-term stratospheric water vapor trends, Commun. Earth Environ., 4, 441, https://doi.org/10.1038/s43247-023-01094-9, 2023.

Tilmes, S., Pan, L. L., Hoor, P., Atlas, E., Avery, M. A., Campos, T., Christensen, L. E., Diskin, G. S., Gao, R.-S., Herman, R. L., Hintsa, E. J., Loewenstein, M., Lopez, J., Paige, M. E., Pittman, J. V., Podolske, J. R., Proffitt, M. R., Sachse, G. W., Schiller, C., Schlager, H.,
475   Smith, J., Spelten, N., Webster, C., Weinheimer, A., and Zondlo, M. A.: An aircraft-based upper troposphere and lower stratosphere O_3, CO, and H_2O climatology for the Northern Hemisphere, J. Geophys. Res., 115, D14 303, https://doi.org/10.1029/2009JD012731, 2010.

Tinney, E. N. and Homeyer, C. R.: A 13-year Trajectory-Based Analysis of Convection-Driven Changes in Upper Troposphere Lower Stratosphere Composition Over the United States, J. Geophys. Res. Atmos., 126, e2020JD033 657, https://doi.org/https://doi.org/10.1029/2020JD033657, 2021.

480 Tinney, E. N., Homeyer, C. R., Elizalde, L., Hurst, D. F., Thompson, A. M., Stauffer, R. M., Vömel, H., and Selkirk, H. B.: A Modern Approach to a Stability-Based Definition of the Tropopause, Mon. Weather Rev., 150, 3151 – 3174, https://doi.org/https://doi.org/10.1175/MWR-D-22-0174.1, 2022.

von Hobe, M., Ploeger, F., Konopka, P., Kloss, C., Ulanowski, A., Yushkov, V., Ravegnani, F., Volk, C. M., Pan, L. L., Honomichl, S. B., Tilmes, S., Kinnison, D. E., Garcia, R. R., and Wright, J. S.: Upward transport into and within the Asian monsoon anticyclone as inferred 485 from StratoClim trace gas observations, Atmos. Chem. Phys., 21, 1267–1285, https://doi.org/10.5194/acp-21-1267-2021, 2021.

World Meteorological Organization: A three-dimensional science: Second session of the commission for aerology, 1957.

Yu, W., Garcia, R., Yue, J., Russell III, J., and Mlynczak, M.: Variability of Water Vapor in the Tropical Middle Atmosphere Observed From Satellites and Interpreted Using SD-WACCM Simulations, J. Geophys. Res. Atmos., 127, e2022JD036 714, https://doi.org/https://doi.org/10.1029/2022JD036714, e2022JD036714 2022JD036714, 2022.

490 Zhang, J., Kinnison, D., Emmons, L., Honomichl, S., Smith, W. P., Tilmes, S., Wang, X., Franchin, A., Flocke, F., and Pan, L. L.: Sources and Regional Attributions to Upper Troposphere Nitrogen Oxides During the Asian Summer Monsoon 2022, Geophys. Res. Lett., 52, e2024GL114 265, https://doi.org/https://doi.org/10.1029/2024GL114265, e2024GL114265 2024GL114265, 2025.